Supporting information

Polarization field engineering through doping-induced anisotropic distortion for efficient piezo-photocatalysis

Xicheng Li [§a], Bicheng Ji [§a], Xue Wang [a], Pengyuan Liu [a], Changzheng Wang *[a], Haiyan Li *[ab]

[a] Beijing Engineering Research Center of Sustainable Urban Sewage System Construction and Risk Control, Beijing University of Civil Engineering and Architecture, Beijing 100044, China

[b] Beijing Energy Conservation & Sustainable Urban and Rural Development Provincial and Ministry Co-construction Collaboration Innovation Center, Beijing University of Civil Engineering and Architecture, Beijing 100044, China

* Corresponding authors.

E-mail addresses: changzhwang@163.com (Changzheng Wang). lihaiyan@bucea.edu.cn (Haiyan Li).

§ These authors contribute equally to this work.

Table of Contents

Supplementary Text

Text S1 The calculation of depletion width (W_b)

The depletion width depends on the band bending in the semiconductor's depletion region and can be calculated using the following equation:

$$W_b = \sqrt{\frac{2\varepsilon\varepsilon_0 V_{FB}}{qN_D}} = \sqrt{\frac{2\varepsilon\varepsilon_0 (E_{OC} - E_{FB})}{qN_D}} \quad \text{Eq.S1}$$

where q is the elementary charge, ε is the dielectric constant of the semiconductor, ε_0 is the vacuum permittivity, N_D is the carrier concentration, E_{OC} is the open-circuit potential at dark equilibrium, and E_{FB} represents the flat-band potential [1].

Text S2 Internal electric field （IEF） intensity

According to Le Formal and Grätzel, the internal electric field is proportional to the surface accumulated charge, obtained by integrating the transient photocurrent density minus its steady-state value over time. The IEF of the catalyst can be calculated based on Kanata et al. [2–4]:

$$E = \left(\frac{-2V_s\rho}{\varepsilon\varepsilon_0}\right)^{\frac{1}{2}} \quad \text{Eq.S2}$$

where E, V_s, ρ, ε and ε_0 represent the IEF magnitude, surface potential, surface charge density, low-frequency dielectric constant, and vacuum permittivity, respectively.

Text S3 Charge separation efficiency

To measure the photogenerated charge separation efficiency, 0.1 M Na_2SO_3 was used as both the electrolyte and hole scavenger. The separation efficiency (η) was calculated as follows：

$$\eta = J_{SO_4^{2-}} / J_{SO_3^{2-}} \quad \text{Eq.S3}$$

where $J_{SO_4^{2-}}$ and $J_{SO_3^{2-}}$ are the photocurrent densities measured under different electrolyte conditions [5].

Text S4 Synergistic factor

The synergistic factor (SF) was used to evaluate the cooperative effect between piezo- and photocatalysis:

$$SF = \frac{K_{app}(piezo - photocatalysis)}{K_{app}(piezocatalysis) + K_{app}(photocatalysis)} \quad \text{Eq.S4}$$

where K_{app} represents the apparent rate constants under the three catalytic conditions. SF < 1 indicates a negative interaction, SF > 1 indicates a positive interaction, and SF = 1 indicates no significant correlation.

Text S5 Escherichia coli growth inhibition experiment

The antibacterial activity of tetracycline hydrochloride (TCH) against *Escherichia coli* (ATCC 25922) was evaluated using the Oxford cup method [6]. In brief, sterile LB agar plates were inoculated with 1 mL of bacterial suspension (OD_{600} = 1). Three Oxford cups (6 mm in diameter) were placed on each plate, and 200 μL of the sample was added to each cup. Plates were incubated at 30°C for 24 h. The residual antibacterial activity of TCH at different treatment stages was assessed by comparing the inhibition zones.

Text S6 First-principles calculations

The first principles calculation uses DFT via the Vienna ab initio simulation package (VASP) package and projector enhanced wave (PAW) method, employing generalized gradient approximation (GGA) by Perdew Burke Ernzerhof (PBE) for electron exchange.[7] In order to make the calculation results reasonable, the plane wave basis has a 490 eV energy cutoff, with a convergence threshold of 10^{-5} eV and a force convergence of 0.03 eV $Å^{-1}$ for structural optimization. A 3 × 3 × 1 k-point grid centered on gamma is used in the Brillouin zone. A 15 Å vacuum is added to prevent plate interactions. $Bi_4Ti_3O_{12}$ (001) (BTO) and La-$Bi_4Ti_3O_{12}$ (LBTO) structures, consisting of 7 atomic layers and a 15 Å vacuum, were constructed, with defect models generated by removing oxygen atoms from the Bi–O–Ti layers. The bottom four atomic layers were fixed, while the remaining layers were allowed to relax.

Text S7 Quantum chemistry calculations

The regioselectivity of ROS attacks on TCH molecules is explained based on the Fukui index. Specifically, the Fukui function plays an important role in DFT calculation

and is widely used to predict reaction sites for electrophilic, nucleophilic, and radical attacks. Fukui function was defined as:

$$f(r) = \left[\frac{\partial \rho(r)}{\partial N}\right]_v \quad \text{Eq. S5}$$

Where ρ(r) was the electron density at a point r in space, N was electron number in present system, the constant term v in the partial derivative was external potential.[2] In the condensed version of Fukui function, atomic population number was used to represent the amount of electron density distribution around an atom. The condensed Fukui function could be calculated as:

Nucleophilic attack: $f_k^+ = q_N^k - q_{N+1}^k$ Eq. S6

Electrophilic attack: $f_k^- = q_{N-1}^k - q_N^k$ Eq. S7

Radical attack: $f_k^0 = (q_{N-1}^k - q_{N+1}^k)/2$ Eq. S8

Where q^k was the atom charge of atom K at corresponding state, and the values of Fukui index of the reactive sites were usually larger than other regions.

In this study, the isosurfaces and isopotential maps of the Fukui function, frontier molecular orbital and average local ionization energy on the surface of the TCH molecule were visualized by using Multiwfn in combination with VMD [8,9].

Supplementary Figure

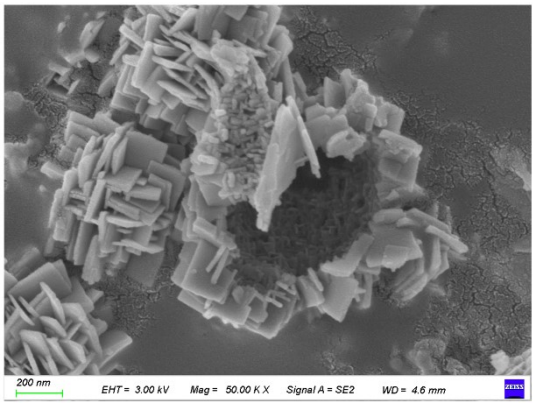

Fig. S1 Scanning electron microscope image of BTO

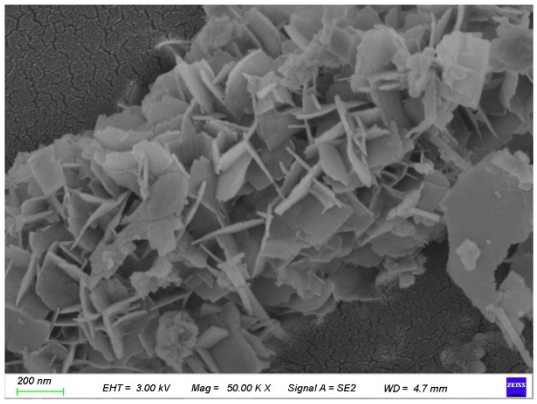

Fig. S2 Scanning Electron Microscope image of LBTO-1.25

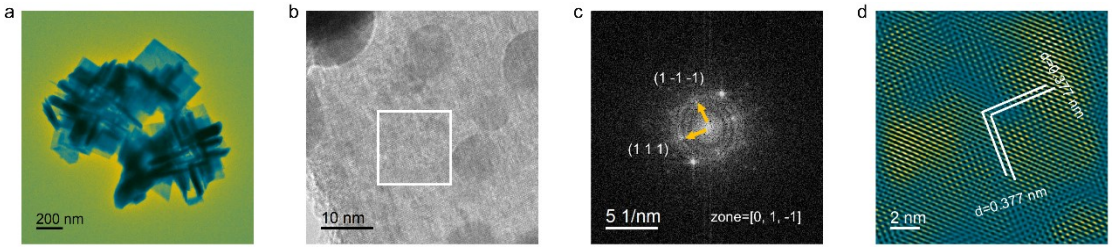

Fig. S3 Transmission electron microscopy images of BTO (a) and HRTEM images (b), fast Fourier transform images (c) and fast inverse Fourier transform images (d).

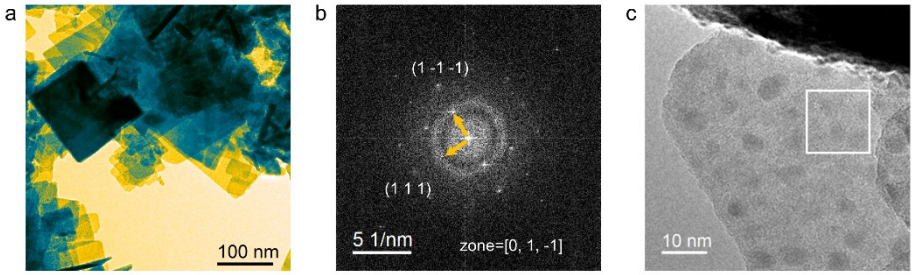

Fig. S4 Fast Fourier Transform image of LBTO-1.25

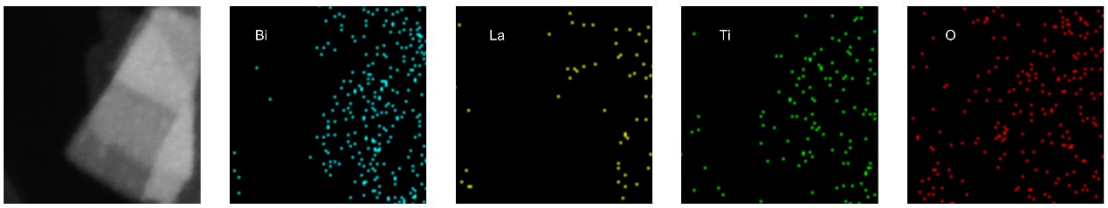

Fig. S5 TEM-EDX elemental mapping of Bi, La, Ti, O in LBTO-1.25

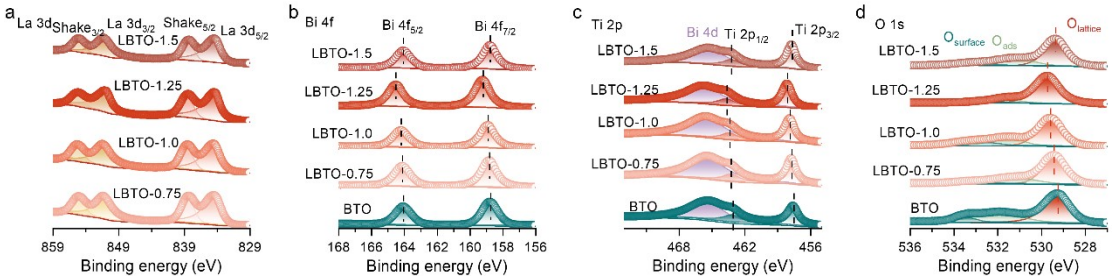

Fig. S6 La 3d (a), Bi 4f (b), Ti 2p (c), and O 1s (d) high-resolution XPS spectrum of LBTO-X (X=0.75, 1.0, 1.25, 1.5) and BTO.

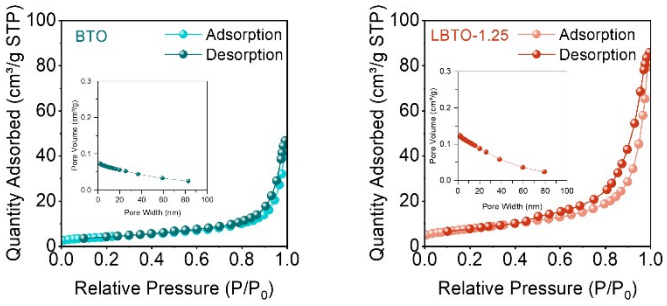

Fig. S7 Nitrogen adsorption and desorption curves of BTO and LBTO-1.25

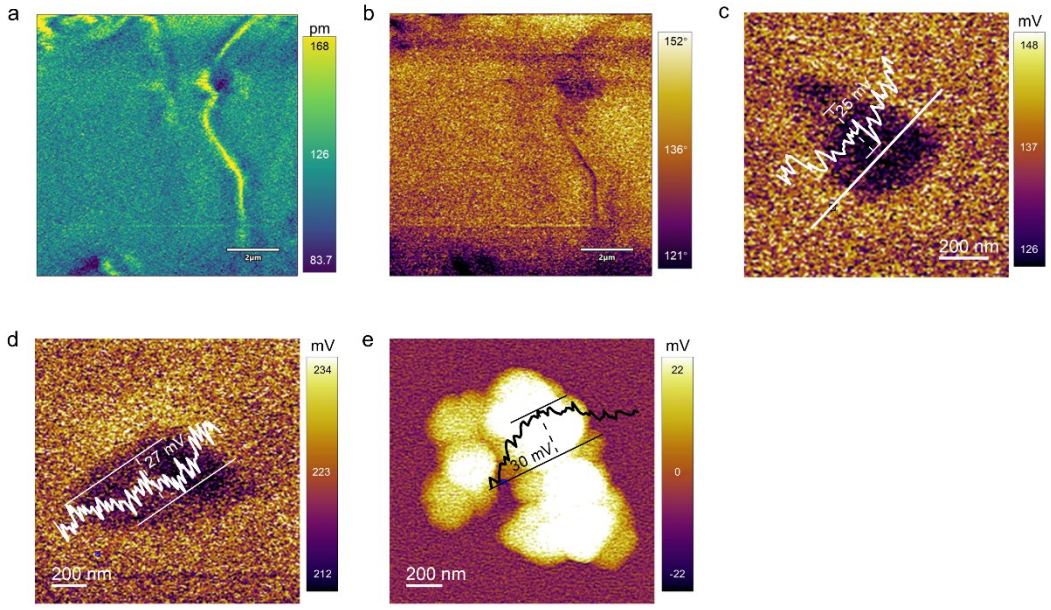

Fig. S8 PFM Amplitude (a), phase (b) and KPFM image (c) of BTO. KPFM image of LBTO-0.75 (d) and LBTO-1.5 (e).

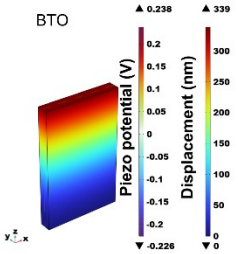

Fig. S9 COMSOL finite element Simulation results of BTO

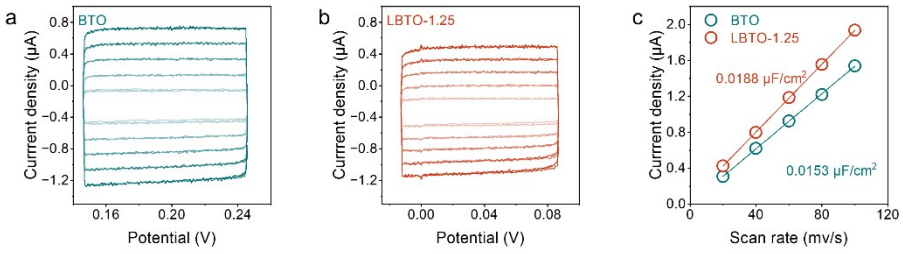

Fig. S10 CV curves (a, b) and active site density (c).

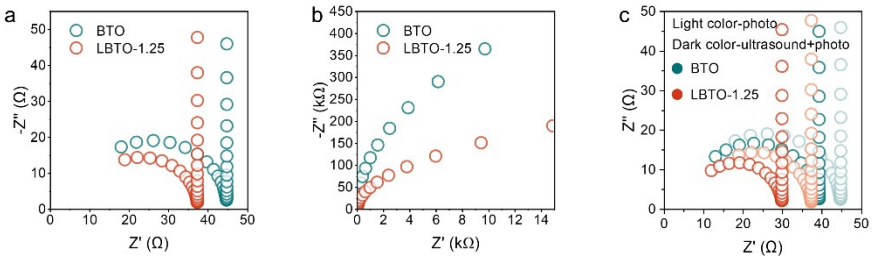

Fig. S11 Nyquist plot of samples: High-frequency part (a), low-frequency part (b), and under different excitation conditions (c).

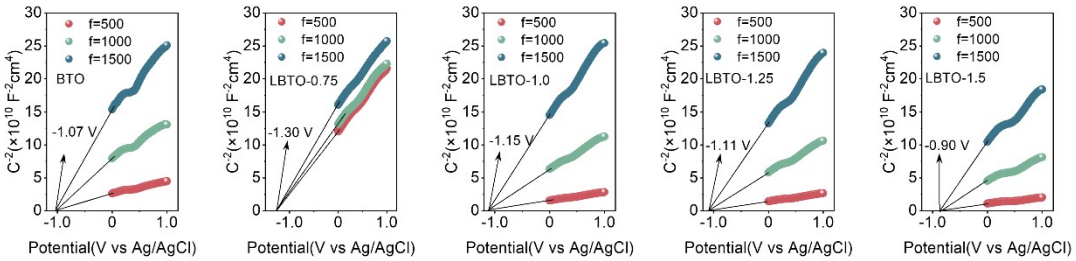

Fig. S12 The Mott-Shottky plot of the sample

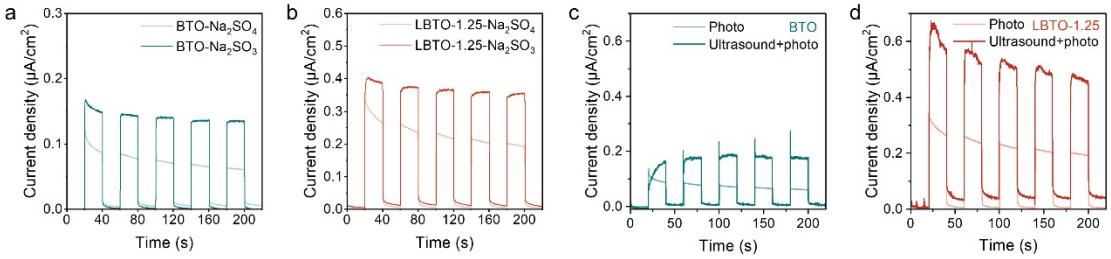

Fig. S13 Photocurrent response results of the samples under different electrolyte conditions: BTO (a), LBTO-1.25 (b). The current densities of BTO (c) and LBTO-1.25 (d) under single photo excitation and ultrasonic-light co-excitation conditions.

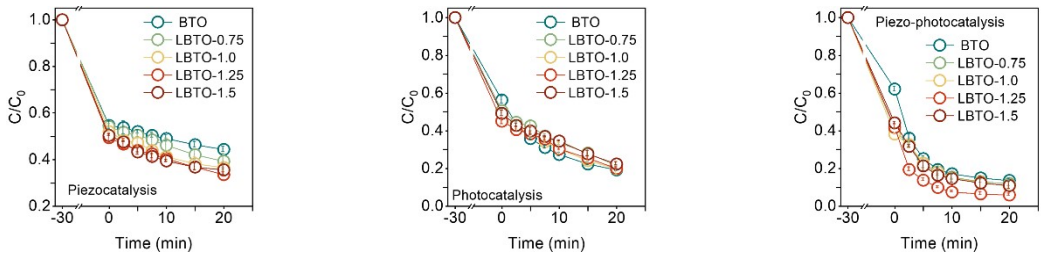

Fig. S14 Degradation performance results of samples with other doping ratios.

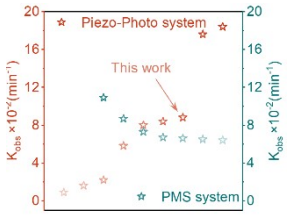

Fig. S15 The comparison chart of degradation rate constants in this work with similar works and the PMS system [10–25].

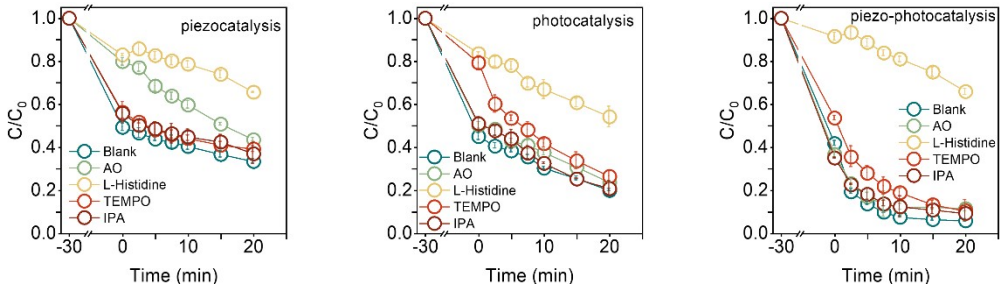

Fig. S16 ROS quenching experiments under different excitation conditions.

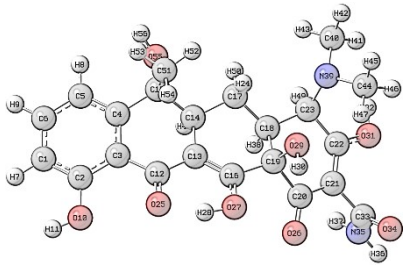

Fig. S17 The optimized TCH molecular structure model.

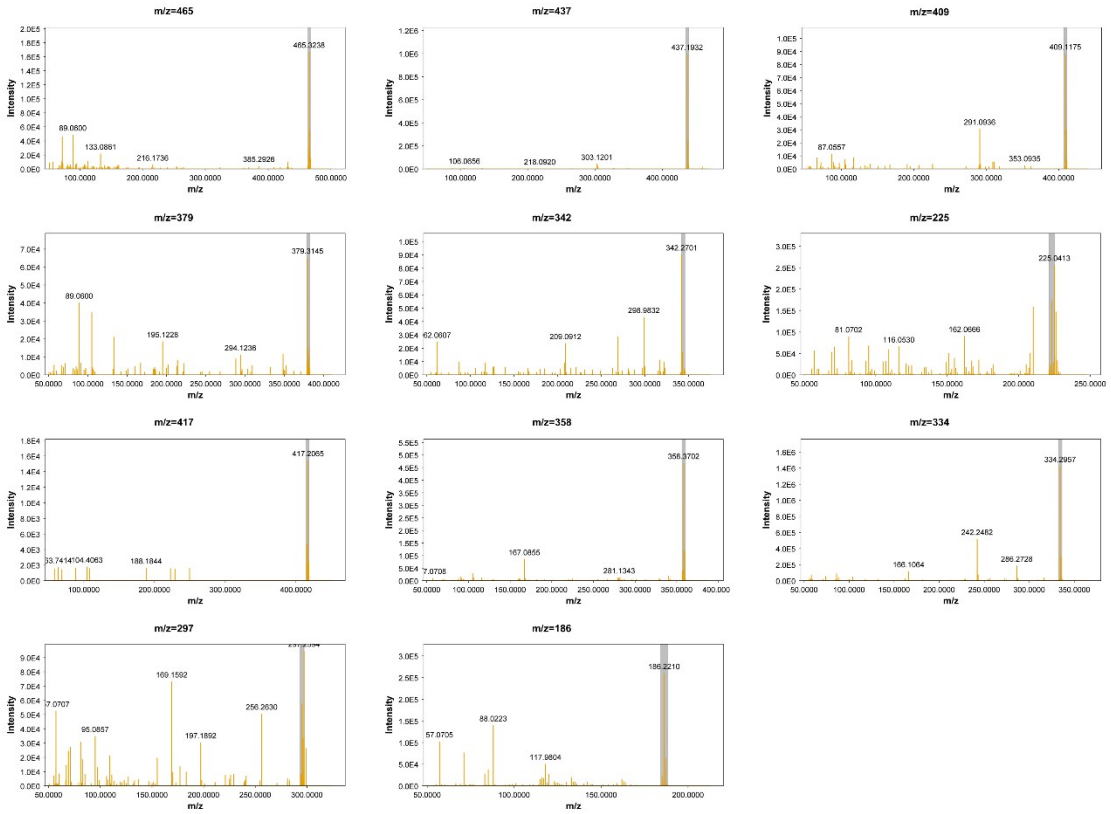

Fig. S18 HPLC-MS results.

Supplementary Table

Table S1 Condensed Fukui function calculation results.

Atom	q(N)	q(N+1)	q(N-1)	f-	f+	f0
1C	-0.0585	-0.0855	-0.0573	0.0012	0.0269	0.0141
2C	0.0878	0.0479	0.089	0.0012	0.0399	0.0206
3C	-0.0367	-0.0611	-0.036	0.0007	0.0244	0.0125
4C	0.0076	-0.0254	0.0082	0.0006	0.033	0.0168
5C	-0.0603	-0.085	-0.0591	0.0012	0.0247	0.013
6C	-0.0219	-0.0781	-0.0205	0.0015	0.0562	0.0288
10O	-0.2046	-0.232	-0.2036	0.0011	0.0273	0.0142
12C	0.1315	0.0149	0.1341	0.0026	0.1166	0.0596
13C	-0.0461	-0.0776	-0.0432	0.0029	0.0314	0.0172

Atom	q(N)	q(N+1)	q(N-1)	f-	f+	f0
14C	-0.0183	-0.0248	-0.0152	0.0031	0.0065	0.0048
15C	0.0939	0.0896	0.0952	0.0013	0.0043	0.0028
16C	0.1079	0.0218	0.1095	0.0016	0.0861	0.0439
17C	-0.0539	-0.0589	-0.0477	0.0061	0.005	0.0056
18C	-0.0162	-0.0196	-0.0008	0.0154	0.0033	0.0094
19C	0.0781	0.0634	0.0818	0.0036	0.0147	0.0092
20C	0.1363	0.1201	0.1476	0.0114	0.0162	0.0138
21C	-0.064	-0.0695	-0.0338	0.0302	0.0055	0.0179
22C	0.1328	0.1229	0.1414	0.0086	0.0099	0.0092
23C	0.0363	0.033	0.0639	0.0275	0.0033	0.0154
25O	-0.2894	-0.4108	-0.2848	0.0046	0.1214	0.063
26O	-0.3444	-0.3702	-0.3152	0.0292	0.0258	0.0275
27O	-0.2012	-0.2679	-0.1971	0.004	0.0667	0.0354
29O	-0.2095	-0.2322	-0.2025	0.007	0.0228	0.0149
31O	-0.1533	-0.1616	-0.1352	0.0181	0.0083	0.0132
33C	0.1522	0.1497	0.1596	0.0074	0.0024	0.0049
34O	-0.4237	-0.4281	-0.4055	0.0183	0.0044	0.0113
35N	-0.1063	-0.1084	-0.1002	0.0061	0.0021	0.0041
39N	-0.0959	-0.0977	0.1561	0.252	0.0018	0.1269
40C	-0.0371	-0.0385	0.0195	0.0566	0.0015	0.029
44C	-0.0556	-0.0574	-0.0006	0.0549	0.0018	0.0284
51C	-0.0885	-0.0944	-0.0877	0.0008	0.0058	0.0033
55O	-0.2417	-0.2509	-0.2404	0.0013	0.0092	0.0052

Supplementary references

[1] C. Li, A. Li, Z. Luo, J. Zhang, X. Chang, Z. Huang, T. Wang, J. Gong, Surviving High-Temperature Calcination: ZrO_2-Induced Hematite Nanotubes for Photoelectrochemical Water Oxidation, Angew. Chem. Int. Ed. 56 (2017) 4150–4155.

[2] P. Lefebvre, J. Allègre, B. Gil, H. Mathieu, N. Grandjean, M. Leroux, J. Massies, P. Bigenwald, Time-resolved photoluminescence as a probe of internal electric fields in GaN-(GaAl)N quantum wells, Phys. Rev. B 59 (1999) 15363–15367.

[3] G. Morello, F. Della Sala, L. Carbone, L. Manna, G. Maruccio, R. Cingolani, M. De Giorgi, Intrinsic optical nonlinearity in colloidal seeded grown CdSe/CdS nanostructures: Photoinduced screening of the internal electric field, Phys. Rev. B 78 (2008) 195313.

[4] J. Seo Im, H. Kollmer, J. Off, A. Sohmer, F. Scholz, A. Hangleiter, Reduction of oscillator strength due to piezoelectric fields in $GaN/Al_xGa_{1-x}N$ quantum wells, Phys. Rev. B 57 (1998) R9435–R9438.

[5] L. Liu, J. Hu, Z. Ma, Z. Zhu, B. He, F. Chen, Y. Lu, R. Xu, Y. Zhang, T. Ma, M. Sui, H. Huang, One-dimensional single atom arrays on ferroelectric nanosheets for enhanced CO_2 photoreduction, Nat. Commun. 15 (2024) 305.

[6] M. Čvančarová, M. Moeder, A. Filipová, T. Cajthaml, Biotransformation of fluoroquinolone antibiotics by ligninolytic fungi-Metabolites, enzymes and residual antibacterial activity, Chemosphere 136 (2015) 311–320.

[7] G. Seifert, D. Porezag, Th. Frauenheim, Calculations of molecules, clusters, and solids with a simplified LCAO-DFT-LDA scheme, International Journal of Quantum Chemistry 58 (1996) 185–192.

[8] T. Lu, F. Chen, Multiwfn: A multifunctional wavefunction analyzer, J. Comput. Chem. 33 (2012) 580–592.

[9] T. Lu, A comprehensive electron wavefunction analysis toolbox for chemists, Multiwfn, The J. Chem. Phys. 161 (2024) 082503.

[10] X. Zhao, J. Tong, S. Bai, J. Qian, Dual-metal-catalyzed Fenton-like reaction on $Cd_xZn_{1-x}S$ @biochar: Mechanistic insights into sulfide-metal interactions for water purification, Appl. Catal. B: Environ. Energy 379 (2025) 125654.

[11] Z. Liu, H. Gan, X. Li, S. Xiong, M. Xu, Q. Guo, D. Xue, Synthesis and characterization of Fe_3O_4/ZrO_2 and degradation of tetracycline in water by activated peroxymonosulfate, Chem. Eng. Sci. 317 (2025) 122121.

[12] K. Cui, H. Liu, X. Cao, P. Wu, J. Wang, X. Liu, J. Qiu, Stepwise approach to environmental remediation: Effective Cu^{2+} adsorption and catalytic degradation of tetracycline using red mud and coal gasification slag-based magnetic zeolite LTA, Chem. Eng. J. 519 (2025) 164962.

[13] K. Zhao, A. Labidi, H. Ren, H. Kang, T. Huang, J. Lohwacharin, H. Zheng, A. Zhou, C. Wang, Micro-Nano Bubbles Induced Piezocatalysis with Barium Titanate/Polyvinylidene Fluoride Membrane: Synergistic Mechano-Optical Enhancement for Tetracycline Degradation, ACS EST Eng. (2025) acsestengg.5c00204.

[14] Y. Cheng, T. Yu, X. Lei, J. Li, J. You, X. Liu, R. Guo, Construction of charge transport channels and strong interfacial electric fields in $BiVO_4/Cu_2O$ Type-II heterojunction for enhanced piezo-photocatalytic performance, J. Environ. Chem. Eng. 13 (2025) 116763.

[15] E. Zhao, S. Yang, Z. Zhou, Y. Deng, X. Qi, Y. Liu, L. Liu, C. Yang, Y. Lan, B. Zhao, M. Wang, W. Wang, Oxygen vacancy-enhanced piezo-photocatalytic for tetracycline hydrochloride

degradation in wastewater and H_2 evolution, J. Colloid Interf. Sci. 686 (2025) 359–366.

[16] X. Zheng, Z. Yang, G. Zeng, Q. Lin, X. Chen, Y. Xiang, Y.-H. Chiao, R.R. Gonzales, Z.-X. Low, J. Luo, Enhancing antibiotic removal of mixed matrix membranes through electrostatic surface segregation of MIL-101(Fe) catalysts, Chem. Eng. J. 505 (2025) 159865.

[17] Y. Cheng, T. Yu, X. Lei, B. Wang, W. Mu, X. Liu, R. Guo, Regulation of oxygen vacancy by in-situ piezoelectric synthesized $BiVO_4$ to induce spin polarization for boosting the piezo-photocatalytic activity, Chem. Eng. J. 504 (2025) 158900.

[18] P. Chen, Y. Zhao, C. Li, X. Chen, J. Wang, Interfacial engineering of Fe-O-Zn bonds in heterojunction photocatalysts: synergistic visible light PMS activation and electron transfer efficiency enhancement, J. Mater. Chem. A 13 (2025) 25829–25841.

[19] Y. Cheng, Z. Ni, W. Wang, X. Lei, B. Wang, X. Liu, R. Guo, Photo-induced $BiVO_4$ to produce P25-like structure for enhancing piezo-photocatalytic activity, J. Water Process Eng. 67 (2024) 106195.

[20] H. Wang, Z. Long, R. Chen, H. Zhang, H. Shi, Y. Chen, Boosting PMS activation over $BiVO_4$ piezo-photocatalyst to rapidly degrade tetracycline: Intermediates and mechanism, Sep. Purif. Technol. 331 (2024) 125598.

[21] T. Wu, Z. Liu, B. Shao, Q. He, Y. Pan, X. Zhang, J. Sun, M. He, L. Ge, C. Cheng, T. Hu, Enhanced piezo-photocatalytic degradation of organic pollutants by cambered wall lamellar structure of porous tubular g-C_3N_4, Nano Energy 120 (2024) 109137.

[22] Y. Li, X. Zhang, R. Sha, T. Li, C. Hu, S. Tu, F. Chen, H. Huang, Efficient piezo-photocatalysis of $Bi_2O_2(OH)NO_3$/BiOI heterojunction: Collaboration of piezoelectric polarization and interface electric field, Chem. Eng. J. 480 (2024) 147976.

[23] X. Sun, T. Xu, T. Xian, Z. Yi, G. Liu, J. Dai, H. Yang, Insight on the enhanced piezo-photocatalytic mechanism of In_2O_3/$BiFeO_3$ heterojunctions for degradation of tetracycline hydrochloride, Appl. Surf. Sci. 640 (2023) 158408.

[24] L. Guo, C. Hu, S. Tu, C. Wang, L. Mei, Y. Zhang, H. Huang, Weak force-polarization driven exceptional piezo-photocatalysis by coupling dual-active piezoelectric semiconductors in $NaNbO_3$/g-C_3N_4 heterojunction, Chem. Eng. J. 476 (2023) 146541.

[25] Z. Zhang, Z. Wang, J. Tan, K. Zhou, J.V. Garcia-Meza, S. Song, L. Xia, Yeast-derived biochar to load $CoFe_2O_4$: Degradation of tetracycline hydrochloride by heterogeneous activation of peroxymonosulfate, J. Environ. Chem. Eng. 11 (2023) 110020.